Depósito de investigación de la Universidad de Sevilla

https://idus.us.es/

1 **Zirconium retention for minimizing environmental risk: role**

2 **of counterion and clay mineral.**

3 Laura Montes[a], Esperanza Pavón[a,b], Agustín Cota[c] and María D. Alba[a,1]

4 *[a]Instituto Ciencia de los Materiales de Sevilla (CSIC-US). Avda. Americo Vespucio, 49.*

5 *41092 Sevilla (Spain).*

6 *[b]Departamento de Física de la Materia Condensada. Universidad de Sevilla. Avda. Reina*

7 *Mercedes s/n. 41012 Sevilla (Spain).*

8 *[c]Laboratorio de Rayos-X. CITIUS. Universidad de Sevilla. Avda. Reina Mercedes 4.*

9 *41012 Sevilla (Spain)*

10

11 **Abstract:** Zr(IV) together with U(IV) are the major components of high-level

12 radionuclide waste (HLRW) and spent nuclear fuel (SNF) from nuclear power plants.

13 Thus, their retention in the waste disposal is of great importance for the environmental

14 risk control. Here, the influence of clay minerals on the retention of Zr(IV), as component

15 of the nuclear waste and as chemical analogues of U(IV), has been evaluated. Three clay

16 minerals, two bentonites and one saponite, were hydrothermally treated with three

17 zirconium salts. A structural study at long-range order by X-ray diffraction and short-

18 range order by NMR was performed to evaluate the generation of new zirconium phases

19 and degradation of the clay minerals. Three immobilization mechanisms were observed:

20 i) cation exchange of ZrO^{2+} or Zr^{4+} by clay minerals, ii) the precipitation/crystallization

21 of ZrO_2, and, iii) the chemical interaction of zirconium with the clay minerals, with the

22 formation of zirconium silicates.

23   *Keywords.* Clay minerals; zirconium; uranium; radioactive waste disposal

24

[1] Corresponding author.
E-mail address: alba@icmse.csic.es

1. Introduction

The presence of zirconium, Zr(IV), in nuclear waste and reprocessing of nuclear fuel has been widely studied (Coughtrey et al., 1983). Moreover, due to its relatively short half-life, the isotope ^{89}Zr ($t_{1/2}$ =78.4 h) is considered as a promising candidate for use as a positron-emitting surrogate for ^{90}Y in radioimmunotherapy (Verel et al., 2003), because stable isotopes of that non-essential element have a low order of toxicity for the living organisms (Ghosh et al., 1992). Nevertheless, due to fission reactions, the long half-life isotope ^{93}Zr ($t_{1/2}$=106 years) is found in radioactive wastes (Ghosh et al., 1992).

In addition, uranium is the major component of high-level radionuclide waste (HLRW) and spent nuclear fuel (SNF) from nuclear power plants, thus, it is essential to analyse the safety of its retention in the waste disposal to minimize the environmental risks. Previously, stable analogues of UO^{2+}, ZrO^{2+} chemical simulator, has been employed at laboratory scale (Villa-Alfageme et al., 2015).

Several natural adsorbents have been employed for the treatment of nuclear waste. Clay minerals have high-affinity adsorption for radionuclides and low water permeability (Yapar et al., 2015). High sorption capacity, low water solubility, availability, low cost, high stability under oxidizing and reducing conditions, and high cation exchange capacity (CEC) have made the clays excellent adsorbent materials.

Regarding the adsorption properties of the clay minerals (Pan et al., 2011), recent studies highlight the existence of an additional retention mechanism (Alba et al., 2009a; Trillo et al., 1994). The systematic study of the interaction of the rare earths cations (REE), such as La, Lu, Nd, Sm – as actinides chemical analogues, with natural and artificial clay minerals – revealed a reaction mechanism based on the interaction between the lanthanide cations and the orthosilicate anions of the lamellar structure (Alba et al., 2011; Alba and Chain, 2005, 2005). At subcritical conditions, 374 ºC and 22 MPa,

(Dooley, 2016) an insoluble and chemically stable phase, $REE_2Si_2O_7$, was generated (Alba et al., 2009b). This might provide a stable immobilisation mechanism if the sorption and swelling capacities of the bentonite fail (Alba and Chaín, 2007).

Initial storage temperatures in the deep geological repository (DGR) are expected to be greater than 200 ºC, with temperatures falling below 150 ºC several hundred years after emplacement (Ojovan, M.I.; Lee, 2014; Poinssot et al., 1996a). Pressure in DGR is expected to be below the maximum subcritical pressure conditions used in the hydrothermal treatments, ca. 10.13 MPa. Nevertheless, hydrothermal conditions of high pressure and temperature were used to follow, in reasonable times, the reactions. Thus, many studies have been carried out by simulating the deep geological disposal at temperatures up to 350 ºC to increase the reaction rate (Alba and Chaín, 2007; Beswick et al., 2014; Gibb et al., 2012, 2008; Poinssot et al., 1996a; Savage, D, Chapman, 1982).

Although many studies have corroborated the chemical interactions between actinides with oxidation state +3, few studies have been carried out to analyse this mechanisms with the cations of oxidation state +4 presents on the HLRW and its influence on the retention capacity of bentonites for other radionuclides from HLRW and SNF (Villa-Alfageme et al., 2015). Also, the type of anion present in a background ionic medium had an effect on cation selectivity and specific sorption (Sharma and Sharma, 2013a).

Therefore, the main goal of this study was to examine the influence of clay minerals on the retention of Zr(IV), as component of the nuclear waste and as chemical analogous of U(IV). Then, the potential use of bentonites and a pure saponite for decontamination or retention of HLRW at various environmental solutions were evaluated.

2. Experimental section

2.1. Materials

75 The examined clay minerals were 2:1 phyllosilicates, two bentonites (FEBEX and

76 MX-80) considered as suitable buffer material in HLRW repositories (Rao and Ravi,

77 2013) and one saponite because previous studies demonstrated that trioctahedral

78 smectites with aluminium in tetrahedral sheet enhanced their HLRW retention capacity

79 (Alba et al., 2001, 2001).

80 The FEBEX bentonite was extracted from the Cortijo de Archidona deposit (Almería,

81 Spain). The processing at the factory consisted of disaggregation and gently grinding,

82 drying at 60 °C and sieving by 5 mm (ENRESA, 2006, 2000). The montmorillonite

83 content of the FEBEX bentonite was 90-92 % (Fernandez et al., 2004). Based on chemical

84 analyses, the structural formula or unit-cell formula of the Ca conditioned FEBEX

85 smectite is (Fernandez et al., 2004):

86 $(Ca_{0.5}Na_{0.08}K_{0.11})(Si_{7.78}Al_{0.22})(Al_{2.78}\ Fe^{III}_{0.33}Fe^{II}_{0.02}Mg_{0.81})O_{20}(OH)_4$.

87 The MX-80 bentonite was extracted from Wyoming (USA) and was supplied in the

88 form of powder (Madsen, 1998). The MX-80 batch used in this investigation was mainly

89 composed of montmorillonite (83%) (Villar et al., 2012). Based on chemical analyses,

90 the structural formula or unit-cell formula of MX-80 smectite is (Montes-H et al., 2005):

91 $(Na_{0.36}Ca_{0.20})(Si_{7.96}Al_{0.04})(Al_{3.1}Mg_{0.56}Fe^{III}_{0.18}Fe^{II}_{0.16})O_{20}(OH)_4$.
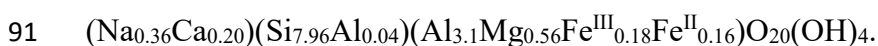
92 Saponite, SapCa-2, has been obtained from the Source Clay Minerals Repository

93 University of Missouri (Columbia) and it has the following chemical formula (Alba et al.,

94 2001): $Na_{0.61}K_{0.02}Ca_{0.09}\ (Si_{7.2}Al_{0.8})^{IV}(Mg_{5.79}Fe_{0.15})^{VI}O_{20}(OH)_4$. Before to be used, the

95 saponite was sodium homoionized.

96 $ZrO(NO_3)_2 \cdot 7H_2O$ (99 % of purity), $Zr(SO_4)_2 \cdot 4.5H_2O$ (99.999 % of purity) and

97 $ZrOCl_2 \cdot 8H_2O$ (98 % of purity), which are commercially available from Sigma-Aldrich,

98 were used in this work as possible chemical analogues of uranyl and tetravalent actinides

99 presents in HLRW (Chapman and Smelllie, 1986).

100

2.2. Hydrothermal reaction

Three hundred milligrams of the above clay minerals were added to 3.65 mmol of zirconium salts (mmol zirconium:mmol smectite 11.2 ± 0.6), suspended in 50 ml of water and heated, in a stainless steel reactor, at 300 ºC for 1 week; the experimental details are summarized in Table 1. The reaction products were collected by filtering, washed with distilled water and dried at room temperature. It is well-known that in geochemical processes of waste degradation and waste/rock interaction, the expected temperatures reach up to about 200 ºC. However, several studies devoted to simulating deep geological disposal conditions use temperatures of up to 350 ºC to increase the reaction rates (Mather et al., 1982; Savage and Chapman, 1982).

2.3. Characterization techniques

X-ray diffraction (XRD) patterns were obtained at the X-ray laboratory (CITIUS, University of Seville, Spain) on a Bruker D8 Advance instrument equipped with a Cu Kα radiation source operating at 40 kV and 40 mA. Diffractograms were obtained in the 2θ range of 3–70° with a step size of 0.015° and a step time of 0.1 s.

Single-pulse (SP) MAS NMR spectra were recorded in the Nuclear Magnetic Resonance Unit at the University of Cordoba (Spain) on a Bruker AVANCE WB400 spectrometer equipped with a multinuclear probe. Powdered sample was packed in 3.2 mm zirconia rotors and spun at 10 kHz. ^{29}Si MAS NMR spectra were acquired at a frequency of 79.49 MHz, using a pulse width of 2.7 µs (π/2 pulse length = 7.1 µs) and delay times of 3 s. ^{27}Al MAS NMR spectra were recorded at 104.26 MHz with a pulse width of 0.92 µs (π/2 pulse length = 9.25 µs) and a delay time of 0.1 s. The chemical shift values were reported in ppm from tetramethylsilane for ^{29}Si and from a 0.1 M $AlCl_3$

125 solution for ^{27}Al. Spectra were simulated using the DMFIT software (Massiot et al.,

126 2002), Gaussian-Lorentzian model was used for all the peaks, and linewidth, position and

127 amplitude were the fitted parameters.

128

129 **3. Results**

130 *3.1. Reactivity of bentonites*

131 The XRD pattern of raw FEBEX and MX-80 (Fig. 1a and 1e) exhibit typical

132 reflections of montmorillonite. The basal spacing d_{001}, which corresponds to a value of

133 about 1.49 nm is associated to the bilayer hydrated Ca^{2+} in the smectite clay interlayer of

134 FEBEX (El Mrabet et al., 2014) and ca. 1.21 nm due mainly to one-layer hydrate typical

135 of monovalent alkaline cations for MX-80 (Grim, 1968). Additionally, reflection of

136 quartz and tridymite are observed being more evident in the XRD pattern of MX-80.

137 The XRD patterns of the reacted FEBEX with Zr^{4+} or ZrO^{2+} (Fig. 1b-d) show the total

138 disruption of the montmorillonite framework and the impurities of quartz and tridymite

139 with the appearance of new crystalline phases. The main observed crystalline phase is

140 baddeleyite, monoclinic ZrO_2, which is accompanied by minor phases such as zircon,

141 $ZrSiO_4$ and cubic ZrO_2. Additionally, reflections of kaolinite are observed in the XRD of

142 the FEBEX treated with $ZrO(NO_3)_2$, Zr-N-FEB-1, and $Zr(SO_4)_2$, Zr-S-FEB-1 (Fig. 1c and

143 1d). Finally, the XRD patterns of Zr-C-FEB-1 and Zr-N-FEB-1 (Fig. 1b and 1c) show a

144 background due to the presence of non-crystalline phases.

145 The XRD patterns of MX-80 after hydrothermal reactions (Fig. 1e-h) show also that

146 the main crystalline phase is baddeleyite, accompanied by minor phases such as kaolinite,

147 $ZrSiO_4$ and cubic ZrO_2. The reaction with $ZrO(NO_3)_2$ and $Zr(SO_4)_2$ (Fig. 1g and 1h)

148 provoke the total disruption of the montmorillonite framework. Whereas, the XRD

149 pattern of Zr-C-MX-1 (Fig. 1f) exhibits small reflection of montmorillonite with a

150 d_{001}=1.40 nm, in agreement with previous data reported for smectites saturated with

151 multivalent cations (Ravina and Low, 1977) and small reflections of the quartz and

152 tridymite. Finally, the XRD patterns of Zr-C-MX-1 and Zr-N-MX-1 (Fig. 1f and 1g) show

153 a background due to the presence of non-crystalline phases.

154 ^{29}Si MAS NMR spectra of the untreated bentonites (Fig. 2a) show two set of signals,

155 the main one is in the range of −100 to −80 ppm and is due to Q^3(mAl), typical

156 environment of smectite, and the second one is in the range of −100 to −115 ppm and is

157 due to Q^4(mAl) of the impurities (Engelhardt, G.; Michel, 1987). The deconvolution

158 parameters of the ^{29}Si MAS NMR spectra (Table 2 and 3) show that the Si smectite

159 environments are different in the two bentonites.

160 For FEBEX bentonite, the smectite contribution to the ^{29}Si MAS NMR spectrum (Fig.

161 2a, left) reaches 90.2%, with two signals at −93.85 ppm, Q^3(0Al), and −87.32 ppm,

162 Q^3(1Al), which are compatible with dioctahedral configuration and isomorphical

163 substitution of Si by Al in the tetrahedral sheet (Alba et al., 2001).

164 The ^{29}Si MAS NMR spectrum of MX80 (Fig. 2a, right) shows a symmetric signal at

165 −93.66 ppm due to Q^3(0Al), reaching 77.8 % of the total Si of the spectrum. The absence

166 of Q^3(1Al) environment is due to the lack of substitution of Si by Al in the tetrahedral

167 sheet. In both bentonites, the ^{29}Si MAS NMR spectra are compatible with their

168 mineralogical composition (Montes-H et al., 2005).

169 The ^{27}Al MAS NMR spectra of the untreated bentonites (Fig. 3a) show a main

170 resonance centred at ca. 0 ppm, due to octahedral Al environment and compatible with

171 the dioctahedral character of both bentonites (Engelhardt, G.; Michel, 1987).

172 Additionally, a small signal between 50 and 70 ppm is observed, due to Al in tetrahedral

173 coordination (Engelhardt, G.; Michel, 1987). In both samples, a signal at 50–70 ppm is

174 made of two resonances; the main one at ca. 57 ppm is due to q^4 environment of

175 impurities, and, the very small one at ca. 65 ppm, in FEBEX, was due to q^3 environment

176 in smectite phase (Engelhardt, G.; Michel, 1987).

177 After the treatment, a complete transformation of the ^{29}Si MAS NMR spectra is

178 observed (Fig. 2b-d).

179 The ^{29}Si MAS NMR spectra after the hydrothermal treatment of both bentonites with

180 ZrOCl$_2$, (Fig. 2b) are characterized with very broad bands.

181 The Zr-C-FEB-1 spectrum is the convolution of four peaks (Table 2). The peak at -

182 95.85 ppm corresponds to the Q^3(0Al) Si environment of the remnant montmorillonite.

183 The absence of Q^3(1Al) and the shifts of Q^3(0Al) indicate the leaching of the tetrahedral

184 aluminium (Alba et al., 2001). The signal at the lowest frequency, ca. 111 ppm,

185 corresponds to the Q^4(0Si) environment typical of tridymite (Mackenzie, H.J.D.; Smith,

186 2002). The two other peaks correspond to zirconium silicate phases. The peak at ca. -81

187 ppm corresponds to zircon, Q^0, (Cota et al., 2013) and accounts with the 1.1 % of the total

188 Si environment. Finally, the peak at ca. 103 ppm corresponds to Si Q^4(1Zr) (Ferreira et

189 al., 2001; Lin and Rocha, 2004; Mackenzie, H.J.D.; Smith, 2002) and accounts with the

190 3.2 % of the total Si environment.

191 Due to the low S/N ratio of the Zr-C-MX-1 spectrum, it is not deconvoluted. It is

192 characterized by a broad symmetric band at ca. 104 ppm that could be interpreted that the

193 main Si environment is Q^4(1Zr) environment (Ferreira et al., 2001; Lin and Rocha, 2004;

194 Mackenzie, H.J.D.; Smith, 2002) although it can not be quantified.

195 The ^{27}Al MAS NMR spectra of Zr-C-FEB-1 and Zr-C-MX-1 (Fig. 3b) are

196 characterized by a broad signal at ca. 0 ppm of aluminium in octahedral coordination

197 (Engelhardt, G.; Michel, 1987) due to the Al in the octahedral sheet of the remnant

198 montmorillonite.

The ^{29}Si MAS NMR spectra after the hydrothermal treatment of both bentonites with ZrO(NO$_3$)$_2$ (Fig. 2c) are characterized by a main narrow signal at high frequency accompanied of broader signals at lower frequency. The spectra are deconvoluted in six peaks (Table 2 and 3). In both bentonites, signals corresponding to zirconium silicates are observed: i) one at ca. 81 ppm of ZrSiO$_4$, 4.4 % for Zr-N-FEB-1 and 3.5 % for Zr-N-MX-1; and; ii) two peaks at ca. -104 ppm and ca. -88 ppm due to Q^4(1Zr) and Q^4(2Zr), respectively. The total Q^4(nZr) is 14.5 % for Zr-N-FEB-1 and 44.6 % for Zr-N-MX-1.

The signal of montmorillonite is absent in Zr-N-MX-1 but a signal at -95 ppm, Q^3(0Al) is observed in Zr-N-FEB-1. In both bentonites, a new Q^3 environment is observed at ca. -91 ppm that corresponds to the transformation of montmorillonite, 2:1 phyllosilicate, to kaolinite, 1:1 phyllosilicate (Mantovani et al., 2009). It accounts with a 66.8 % for Zr-N-FEB-1 and 38.4 % for Zr-N-MX-1.

Finally, signals at ca. -111 ppm for both bentonites and at ca. -108 ppm for MX-80 are observed as due to tridymite and quartz (Mackenzie, H.J.D.; Smith, 2002), respectively.

The hydrothermal treatment of both bentonites resulted in ^{27}Al MAS NMR spectra (Fig. 3c) with a unique aluminium symmetric resonance at ca. 0 ppm, due to six-coordinated aluminium. The position at ca. 0 ppm and the low quadrupolar line shape of the band (symmetry band) are compatible with aluminium in the octahedral sheet of kaolinite (Engelhardt, G.; Michel, 1987). The absence of both tetrahedral resonances is compatible with the disruption of the smectite framework (or its dissolution) and with the dissolution of the q^4 impurities of the initial samples.

Severe damages at short range order are observed after the hydrothermal treatment of bentonites with Zr(SO$_4$)$_2$, being more severe in Zr-S-FEB-1 than in Zr-S-MX-1 (Fig. 2d). No ^{29}Si MAS NMR signal is observed in the Zr-S-FEB-1 spectrum (Fig. 2d, left).

224   However, a very broad symmetric signal is observed at ca. 104 ppm in the Zr-S-MX-1

225   spectrum (Fig. 2d, right), that could be interpreted as the main Si environment

226   corresponded with $Q^4(1Zr)$ environment (Ferreira et al., 2001; Lin and Rocha, 2004;

227   Mackenzie, H.J.D.; Smith, 2002) but the low spectral resolution has not allowed the

228   quantification. The ^{27}Al MAS NMR spectra of both bentonites have a very low S/N ratio

229   and show a very broad band at ca. 0 ppm due to aluminium in octahedral coordination

230   (Engelhardt, G.; Michel, 1987).

231

232   *3.2. Reactivity of saponite*

233   Fig. 4 shows the XRD pattern of the saponite before and after hydrothermal reaction

234   with zirconium species. The original saponite (Fig. 4a) shows a pattern that is made up of

235   the two distinct types of reflections, general and basal reflections. The basal spacing of

236   1.21 nm of saponite corresponds to the one-layer hydrated Na^+ (Grim, 1968).

237   The remnant smectite after the hydrothermal reactions with $ZrOCl_2$ (Fig. 4b), show

238   basal spacing up to 1.41 nm, in agreement with previous data reported for smectites

239   saturated with multivalent cations (Ravina and Low, 1977). Additionally, the XRD

240   patterns show new reflections corresponding to baddeleyite and minor reflections of

241   zircon ($ZrSiO_4$) and cubic ZrO_2.

242   After the hydrothermal treatment with $ZrO(NO_3)_2$ and $Zr(SO_4)_2$, the XRD patterns

243   (Fig. 4c and 4d) show the total disruption of the saponite framework and, in both cases,

244   the XRD patterns match with baddeleyite and zircon. Whereas baddeleyite is the

245   dominant crystalline specie of Zr-N-SAP-1 (Fig. 4c), the dominant crystalline specie of

246   Zr-S-SAP-1 was zircon (Fig. 4d).

247   Finally, the XRD patterns of Zr-C-SAP-1 and Zr-N-SAP-1 (Fig. 4b and 4c) show a

248   background due to the presence of non-crystalline phases.

The ^{29}Si MAS NMR spectrum of the starting saponite (Fig. 5a, left) is characterized by three main signals at −95.8, −90.8 and −85.0 ppm corresponding to $Q^3(mAl)$, $0 \leq m \leq 2$, in an intensity ratio of 10:4.6:0.22 (Alba et al., 2001) (Table 4). From these results, the Si/Al ratio can be calculated (Engelhardt, G, Lohse, U, Lippmaa, E, Tarmak, M, Magi, 1981) as 8.9, which is in good agreement with the chemical composition, Si/Al=9.0. The ^{27}Al MAS NMR spectrum of the untreated saponite (Fig. 5a, right) shows a unique signal centred at 65 ppm due to tetrahedral aluminium, $q^3(3Si)$ (Engelhardt, G.; Michel, 1987).

When the saponite is hydrothermally treated ZrOCl$_2$ (Fig. 5b, left), the main ^{29}Si signal is centred at ca. −95 ppm, $Q^3(0Al)$ with a broad band in the chemical shift range of $Q^3(1Al)$, in an intensity ratio 10:5.5. The deconvolution of the spectrum (Table 4) shows a signal at ca. -81 ppm corresponding to zircon accounting with the 4.3 % of the total Si environment and might be due to the chemical reaction of ZrO^{2+} with the saponite. The two sets of signals at ca. 60 ppm and ca. 0 ppm, in the ^{27}Al MAS NMR spectrum (Fig. 5b, right), indicate the partial conversion of the aluminium from tetrahedral to octahedral coordination (Engelhardt, G.; Michel, 1987).

The ^{29}Si MAS NMR spectrum of Zr-N-SAP-1 (Fig. 5c, left) is characterized by a broad band in the range between -120 and -70 ppm. This band is the convolution of six peaks (Table 4). The peak at ca. -82 ppm corresponds to zircon (Cota et al., 2013) and accounts with the 10.7 % of the total Si environment. And the four peaks at lower chemical shifts correspond to Si $Q^4(mZr)$, $0 \leq m \leq 2$, (Ferreira et al., 2001; Lin and Rocha, 2004; Mackenzie, H.J.D.; Smith, 2002); those zeolites were not observed by XRD because they are amorphous. The ^{27}Al MAS NMR spectrum (Fig. 5c, right) is characterized by a narrow signal at ca. 0 ppm due to aluminium in octahedral coordination (Engelhardt, G.; Michel, 1987) and corroborates the total disruption of the saponite framework as previously observed by XRD.

274   Finally, the ^{29}Si MAS NMR spectrum of Zr-S-SAP-1 (Fig. 5d, left) is characterized

275   by a broad symmetric band at ca. -81 ppm corresponds to zircon (Cota et al., 2013) and

276   accounts with the 100 % of the total Si environment. No signal in the ^{27}Al MAS NMR

277   spectrum (Fig. 5d, right) is observed due to the total breakdown of the saponite framework

278   and leaching of the aluminium to the supernatant.

279

280   **4. Discussion**

281   After the hydrothermal treatment, in general, the main phase was ZrO_2, as previously

282   reported for the heating of zirconium salt solutions (Kim and Kim, 1995). The monoclinic

283   polymorph is more abundant than the cubic one (Fig. 1 and 4). The prevalence of the

284   monoclinic polymorph is in good agreement with the stability range of ZrO_2 observed in

285   the thermal decomposition of zirconium salts to generate ZrO_2 (Stefanic et al., 1996).

286   The precipitation of Zr as oxide was accompanied by the disruption of the smectite

287   framework that generated amorphous phases as noticed by the background of the XRD

288   patterns (Fig. 1 and 4). In the case of bentonites, the original montmorillonite was

289   transformed to kaolinite, as previously observed in bentonites that reacted with chemical

290   analogous of actinides (Osuna et al., 2015). Other additional effects on the remnant

291   smectites were: i) the swelling of the interlayer space associated to the replacement of

292   original monovalent and/or divalent cations by trivalent cations leached from the

293   framework , as observed by ^{27}Al MAS NMR (Fig. 3 and Fig. 5 right), or tetravalent

294   cations from zirconium solutions, ZrO^{2+} or Zr^{4+}; and; ii) the dissolution of the impurities

295   (quartz and tridymite), as previously reported in acid hydrothermal treatment (Osuna et

296   al., 2015).

297   The disruption of 2:1 phyllosilicate structure is quantified by ^{29}Si MAS NMR (Tables

298   2, 3 and 4) and it depends on the clay mineral stability in acid media and on the reaction

299   degree. In the case of bentonites, the montmorillonite was transformed to kaolinite and

300   generated zirconium silicates such as orthosilicates, Q^0, and tectosilicates, Q^4. The

301   amount of remnant montmorillonite was higher in Zr-N-FEB-1 than in Zr-N-MX-1, but

302   the transformation to kaolinite was higher in FEBEX, probably due to its higher content

303   on montmorillonite. In the case of FEBEX, the formation of zirconium silicates was lower

304   due to its higher transformation in kaolinite because crystallization of different secondary

305   phases such as the oxide of zirconium instead of silicates is favoured in presence of

306   kaolinite (Poinssot et al., 1996b). The lower octahedral isomorphic substitution of the

307   montmorillonite component of MX80 and the presence of Na^+ instead of Ca^{2+} in its

308   interlayer space seem to favour the chemical reaction of bentonite with zirconium (Osuna

309   et al., 2015).

310   The reaction progress of saponite in $ZrOCl_2$ was similar to bentonite FEBEX (Table

311   2 and 3), ca. 4.3 % of zirconium silicate was formed. The reaction of saponite with

312    $ZrO(NO_3)_2$ and $Zr(SO_4)_2$ produced a 100 % of Si reaction to form zirconium silicate. For

313   Zr-N-SAP-1 the main silicate was a tectosilicate and a orthosilicate, $ZrSiO_4$, was the

314   unique silicate formed for Zr-S-SAP-1. In any case, the reactivity of saponite to form

315   zirconium silicate was higher than for bentonites due to tetrahedral substitutions and the

316   trioctahedral character of the smectite (Alba et al., 2001, 2001).

317   Sharma and Sharma (Sharma and Sharma, 2013b) reported that the type of anion

318   present in a background ionic medium had an effect on cation selectivity and specific

319   sorption of inorganic anions could modulate the negative surface charge, and, then its

320   reactivity. Here, the phase evolution was also influenced by the counterion; the SO_4^{2-}

321   favoured the formation of zirconium silicates (Fig. 4d and 5d) whereas Cl^- and NO_3^-

322   favoured the formation of ZrO_2 (Fig. 4b, 4c, 5b and 5c). It was reported by Bleier and

323   Cannon (Bleier, A.; Cannon, 1986) that the nuclei and primary crystallites of hydrous

324 ZrO$_2$ are formed through the bridging of zirconium species by OH ligands in ZrOCl$_2$ or

325 ZrO(NO$_3$)$_2$ solutions and particles of hydrous ZrO$_2$ are subsequently precipitated through

326 the aggregation of these crystallites.

327

328 **5. Conclusions**

329 The structural analysis has demonstrated that the hydrothermal treatment not only

330 caused the cation exchange of ZrO^{2+} or Zr^{4+} by clay minerals, but also two other

331 mechanisms, the precipitation/crystallization of ZrO$_2$ and the chemical interaction with

332 the clay minerals, with the formation of zirconium silicates, were involved.

333 The nature of the clay and the counterion influences the main retention mechanisms,

334 precipitation and chemical reaction, and the structure of the new zirconium phases.

335 Thus, the formation of new zirconium insoluble phases, oxides and silicates, points

336 out the efficiency of the clay mineral barrier for the building of a safe HLRW disposal.

337

338 **Declaration of Competing Interest**

339 The authors declare that they have no known competing financial interests or personal

340 relationships that could have appeared to influence the work reported in this paper.

341

347

348 **References**

349 Alba, M.D., Becerro, A.I., Castro, M.A., Perdigón, A.C., 2001. Hydrothermal reactivity
350   of Lu-saturated smectites: Part II. A short-range order study. Am. Mineral. 86, 124–
351   131.

352 Alba, M.D., Castro, M.A., Chaín, P., Hurtado, S., Orta, M.M., Pazos, M.C., Villa, M.,
353   2011. Interaction of Eu-isotopes with saponite as a component of the engineered
354   barrier. Appl. Clay Sci. 52, 253–257.

355 Alba, M.D., Chain, P., 2005. Interaction between Lu cations and 2:1 aluminosilicates
356   under hydrothermal treatment. Clays Clay Miner. 53, 37–44.

357 Alba, M.D., Chaín, P., 2007. Persistence of lutetium disilicate. Appl. Geochemistry 22,
358   192–201.

359 Alba, M.D., Chain, P., Orta, M.M., 2009a. Chemical reactivity of argillaceous material
360   in engineered barrier. Rare earth disilicate formation under subcritical conditions.
361   Appl. Clay Sci. 43, 369–375.

362 Alba, M.D., Chain, P., Orta, M.M., 2009b. Rare-earth disilicate formation under Deep
363   Geological Repository approach conditions. Appl. Clay Sci. 46, 63–68.

364 Bergaya, F.; Theng, B.K.G.; Lagaly, G., 2006. Handbook of Clay Science. Elsevier.

365 Beswick, A.J., Gibb, F.G.F., Travis, K.P., 2014. Deep borehole disposal of nuclear waste:
366   engineering challenges. Proc. Inst. Civ. Eng. 167, 47–66.

367 Bleier, A.; Cannon, R.M., 1986. Better ceramics through chemistry Title. Pittsburg.

368 Chapman, N.A., Smelllie, J.A.T., 1986. Special issue - Natural analogs to the conditions
369   around a final repository for high-level radioactive-waste - Introduction and
370   summary of the workshop. Chem. Geol. 55, 167–173.

371 Cota, A., Burton, B.P., Chaín, P., Pavón, E., Alba, M.D., 2013. Solution properties of the
372   system ZrSiO4-HfSiO4: A computational and experimental study. J. Phys. Chem. C
373   117, 10013–10019.

374   Coughtrey, P.J., Jackson, D., Thorne, M.C., 1983. Radionuclide distribution and transport

375   in terrestrial and aquatic ecosystems: a critical review of data. Volume 3. Radionucl.

376   Distrib. Transp. Terr. Aquat. Ecosyst. a Crit. Rev. data. Vol. 3.

377   Dooley, R.B., 2016. Guideline on the Use of Fundamental Physical Constants and Basic

378   Constants of Wateritle. Int. Assoc. Prop. Water Steam G5-01.

379   El Mrabet, S., Castro, M.A., Hurtado, S., Orta, M.M., Pazos, M.C., Villa-Alfageme, M.,

380   Alba, M.D., 2014. Effect of clays and metal containers in retaining Sm^{3+} and ZrO^{2+}

381   and the process of reversibility. Am. Mineral. 99, 696–703.

382   Engelhardt, G, Lohse, U, Lippmaa, E, Tarmak, M, Magi, M., 1981. Si-29 NMR

383   investigations of silicon-aluminum ordering in the aluminosilicate framework of

384   faujasite-type zeolites. Zeitschrift fur Anorg. und Allg. Chemie 478, 239–240.

385   Engelhardt, G.; Michel, D., 1987. High Resolution Solid State NMR of Silicates and

386   Zeolites. John Wiley and Sons, New York.

387   ENRESA, 2006. Full-scale engineered barriers experiment. Madrid.

388   ENRESA, 2000. Full-scale Engineered Barriers Experiment for a Deep Geological

389   Repository for High Level Radioactive Waste in Crystalline Host Rock. Madrid.

390   Fernandez, A.M., Baeyens, B., Bradbury, M., Rivas, P., 2004. Analysis of the porewater

391   chemical composition of a Spanish compacted bentonite used in an engineered

392   barrier. Phys. Chem. Earth 29, 105–118.

393   Ferreira, P., Ferreira, A., Rocha, J., Soares, M.R., 2001. Synthesis and structural

394   characterization of zirconium silicates. Chem. Mater. 13, 355–363.

395   Ghosh, S., Sharma, A., Talukder, G., 1992. Zirconium - An abnormal trace-element in

396   biology. Biol. Trace Elem. Res. 35, 247–271.

397   Gibb, F.G.F., Travis, K.P., Hesketh, K.W., 2012. Deep borehole disposal of higher burn

398   up spent nuclear fuels. Mineral. Mag. 76, 3003–3017.

399 Gibb, F.G.F., Travis, K.P., McTaggart, N.A., Burley, D., Hesketh, K.W., 2008. Modeling

400   temperature distribution around very deep borehole disposals of HLW. Nucl.

401   Technol. 163, 62–73.

402 Grim, R.E., 1968. Clay Mineralogy. New York.

403 Kim, D.J., Kim, H., 1995. Effect of zirconium salts on the hydrous ZrO2 coating of sic

404   whiskers. Mater. Lett. 23, 113–116.

405 Lin, Z., Rocha, J., 2004. Small-pore framework zirconium and hafnium silicates with the

406   structure of mineral tumchaite. Microporous Mesoporous Mater. 76, 99–104.

407 Mackenzie, H.J.D.; Smith, M.E., 2002. Multinuclear Solid-State NMR of Inorganic

408   Materials. Pergamon Materials Series, Amsterdam.

409 Madsen, F.T., 1998. Clay mineralogical investigations related to nuclear waste disposal.

410   CLAY Miner. 33, 109–129.

411 Mantovani, M., Escudero, A., Alba, M.D., Becerro, A.I., 2009. Stability of phyllosilicates

412   in Ca(OH)2 solution: Influence of layer nature, octahedral occupation, presence of

413   tetrahedral Al and degree of crystallinity. Appl. Geochemistry 24, 1251–1260.

414 Massiot, D., Fayon, F., Capron, M., King, I., Le Calve, S., Alonso, B., Durand, J.O.,

415   Bujoli, B., Gan, Z.H., Hoatson, G., 2002. Modelling one- and two-dimensional solid-

416   state NMR spectra. Magn. Reson. Chem. 40, 70–76.

417 Mather, J.D., Chapman, N.A., Black, J.H., Lintern, B.C., 1982. The geological disposal

418   of high-level radioactive-waste - A review of the institute of geological sciences

419   research-program. Nucl. Energy-Journal Br. Nucl. Energy Soc. 21, 167–173.

420 Montes-H, G., Fritz, B., Clement, A., Michau, N., 2005. Modelling of geochemical

421   reactions and experimental cation exchange in MX80 bentonite. J. Environ. Manage.

422   77, 35–46.

423 Ojovan, M.I.; Lee, W.E., 2014. Performance Assessment, An Introduction to Nuclear

424   Waste Immobilisation. Amsterdam.

425   Osuna, F.J., Chain, P., Cota, A., Pavón, E., Alba, M.D., 2015. Impact of hydrothermal

426   treatment of FEBEX and MX80 bentonites in water, HNO3 and Lu(NO3)3 media:

427   Implications for radioactive waste control. Appl. Clay Sci. 118, 48–55.

428   Pan, D., Fan, Q., Li, P., Liu, S., Wu, W., 2011. Sorption of Th(IV) on Na-bentonite:

429   Effects of pH, ionic strength, humic substances and temperature. Chem. Eng. J. 172,

430   898–905.

431   Poinssot, C., Goffe, B., Magonthier, M.C., Toulhoat, P., 1996a. Hydrothermal alteration

432   of a simulated nuclear waste glass: Effects of a thermal gradient and of a chemical

433   barrier. Eur. J. Mineral. 8, 533–548.

434   Poinssot, C., Goffe, B., Magonthier, M.C., Toulhoat, P., 1996b. Hydrothermal alteration

435   of a simulated nuclear waste glass: Effects of a thermal gradient and of a chemical

436   barrier. Eur. J. Mineral. 8, 533–548.

437   Rao, S.M., Ravi, K., 2013. Hydro-mechanical characterization of Barmer 1 bentonite

438   from Rajasthan, India. Nucl. Eng. Des. 265, 330–340.

439   Ravina, I., Low, P.F., 1977. Change of b-dimension with swelling of montmorillonite.

440   Clays Clay Miner. 25, 201–204.

441   Savage, D, Chapman, N.A., 1982. Hydrothermal behavior of simulated waste glass and

442   waste rock interactions under repository conditions. Chem. Geol. 36, 59–86.

443   Savage, D., Chapman, N.A., 1982. Hydrothermal behavior of simulated waste glass and

444   waste rock interactions under repository conditions. Chem. Geol. 36, 59–86.

445   Sharma, V., Sharma, K.N., 2013a. Influence of Accompanying Anions on Potassium

446   Retention and Leaching in Potato Growing Alluvial Soils. Pedosphere 23, 464–471.

447   Sharma, V., Sharma, K.N., 2013b. Influence of Accompanying Anions on Potassium

448   Retention and Leaching in Potato Growing Alluvial Soils. Pedosphere 23, 464–471.

449 Stefanic, G., Music, S., Popovic, S., Furic, K., 1996. Formation of ZrO2 by the thermal

450   decomposition of zirconium salts. Croat. Chem. Acta 69, 223–239.

451 Trillo, J.M., Alba, M.D., Alvero, R., Castro, M.A., Muñoz-Páez, A., Poyato, J., 1994.

452   Interaction of Multivalent Cations with Layered Clays. Generation of Lutetium

453   Disilicate upon Hydrothermal Treatment of Lu-Montmorillonite. Inorg. Chem. 33,

454   3861–3862.

455 Verel, I., Visser, G.W.M., Boerman, O.C., van Eerd, J.E.M., Finn, R., Boellaard, R.,

456   Vosjan, M., Walsum, M.S. V, Snow, G.B., van Dongen, G., 2003. Long-lived

457   positron emitters zirconium-89 and iodine-124 for scouting of therapeutic

458   radioimmunoconjugates with PET. Cancer Biother. Radiopharm. 18, 655–661.

459 Villa-Alfageme, M., Hurtado, S., El Mrabet, S., Pazos, M.C., Castro, M.A., Alba, M.D.,

460   2015. Uranium immobilization by FEBEX bentonite and steel barriers in

461   hydrothermal conditions. Chem. Eng. J. 269, 279–287.

462 Villar, M. V, Gomez-Espina, R., Gutierrez-Nebot, L., 2012. Basal spacings of smectite

463   in compacted bentonite. Appl. Clay Sci. 65–66, 95–105.

464 Yapar, S., Ozdemir, G., Fernandez Solarte, A.M., Torres Sanchez, R.M., 2015. Surface

465   and interface properties of lauroyl sarcosinate-adsorbed CP+-montmorillonite.

466   Clays Clay Miner. 63, 110–118.

467

Table 1

Samples and experimental variables

samples	adsorbent			Zirconium source			pH	g salt
	Saponite	FEBEX	MX80	ZrOCl$_2$	ZrO(NO$_3$)$_2$	Zr(SO$_4$)$_4$		
Zr-N-SAP-1	✓				✓		1.4	1.303
Zr-N-FEB-1		✓			✓		1.4	1.303
Zr-N-MX-1			✓		✓		1.4	1.303
Zr-C-SAP-1	✓			✓			1.4	1.175
Zr-C-FEB-1		✓		✓			1.4	1.175
Zr-C-MX-1			✓	✓			1.4	1.175
Zr-S-SAP-1	✓					✓	1.0	1.330
Zr-S-FEB-1		✓				✓	1.0	1.330
Zr-S-MX-1			✓			✓	1.0	1.330

Table 2

^{29}Si MAS NMR fit parameters of FEBEX before and after treatments

samples	δ (ppm)	Fwhh (Hz)	%	assignation
FEB	-87.3±0.1	200±33	5.0±0.6	Q^3(1Al)
	-93.85±0.01	391±2	85±1	Q^3(0Al)
	-108.52±0.09	461±23	9.8±0.4	quartz
Zr-C-FEB-1	-81.06±0.1	140±25	1.1±0.1	zircon
	-95.9±0.1	1187±19	69±1	Q^3(0Al)
	-102.9±0.2	304±56	3.2±0.9	Q^4(1Zr)
	110.9±0.2	1034±32	26.6±0.9	tridymite
Zr-N-FEB-1	-82±2	1033±164	4.4±0.5	zircon
	-88.5±0.5	542±138	10±1	Q^4(2Zr)
	-91.05±0.01	168±5	67±5	kaolinite
	-95.0±0.1	281±42	9±1	Q^3(0Al)
	-103.4±0.4	613±109	4.3±0.4	Q^4(1Zr)
	-111.1±0.2	421±48	4.8±0.5	tridymite
Zr-S-FEB-1	n.s.	--	--	--

n.s.= not signal

Table 3.

^{29}Si MAS NMR fit parameters of MX-80 before and after treatments

samples	δ (ppm)	Fwhh (Hz)	%	assignation
MX	-93.66±0.02	727±4	77.8±0.3	Q^3(0Al)
	-101.4±0.1	257±29	2.6±0.3	Q^4
	-107.83±0.02	111±7	4.7±0.5	quartz
	-109.64±0.05	240±7	15.0±0.5	tridymite
Zr-C-MX-1	--	v.b	--	--
Zr-N-MX-1	-82.0±0.5	626±109	3.5±0.7	zircon
	-91.22±0.01	159.5±1.4	38.4±0.5	kaolinite
	-91.50±0.06	778±22	41.0±0.9	Q^4(2Zr)
	-103.5±0.1	330±44	3.6±0.4	Q^4(1Zr)
	-107.58±0.02	166±7	7.3±0.3	quartz
	-110.87±0.08	297±16	6.1±0.3	tridymite
Zr-S-MX-1	--	v.b	--	--

v.b.= very broad

Table 4.

^{29}Si MAS NMR fit parameters of saponite before and after treatments

samples	δ (ppm)	Fwhh (Hz)	%	assignation
SAP	-85.9±0.2	588±31	1.5±0.3	Q^3(2Al)
	-90.80±0.01	645±6	31.1±0.3	Q^3(1Al)
	-95.78±0.01	196±11	67.4±0.2	Q^3(0Al)
Zr-C-SAP-1	-81.4±0.1	455±37	4.3±0.3	zircon
	-90.79±0.06	516±12	34±1	Q^3(1Al)
	-95.54±0.02	381±3	61.8±0.9	Q^3(0Al)
Zr-N-SAP-1	-82.1±0.2	533±21	10.7±0.7	zircon
	-85.4±0.1	207±45	3.2±0.7	Q^4(2Zr)
	-92.9±0.1	843±27	24±2	Q^4(2Zr)
	-101.6±0.1	947±39	27±2	Q^4(1Zr)
	-110.57±0.05	761±8	36±2	Q^4(0Zr)
Zr-S-SAP-1	-82.09±0.07	1678±15	100.0±0.0	zircon

CAPTION OF FIGURES

Fig. 1. XRD of bentonite FEBEX and MX-80, before and after the hydrothermal treatment in presence of zirconium aqueous solution: a) FEB; b) Zr-C-FEB-1; c) Zr-N-FEB-1; d) Zr-S-FEB-1; e) MX; f) Zr-C-MX-1; g) Zr-N-MX-1; and; h) Zr-S-MX-1. *=zircon ($ZrSiO_4$) PDF 04-007-5058; o=cubic ZrO_2 PDF 04-015-0098; k=kaolinite PDF 00-001-0527; b=baddeleyite (monoclinic ZrO_2) PDF 00-037-1484; t=tridymite PDF 04-011-3620; and; q=quartz PDF 00-003-0419.

Fig. 2. ^{29}Si MAS NMR spectra of bentonite FEBEX (left) and MX-80 (right) before and after the hydrothermal treatment in presence of a zirconium aqueous solution: a) FEB or MX-80; b) Zr-C-FEB-1 or Zr-C-MX-1; c) Zr-N-FEB-1 or Zr-N-MX-1; and; d) Zr-S-FEB-1 or Zr-S-MX-1.

Fig. 3. ^{27}Al MAS NMR spectra of bentonite FEBEX (left) and MX-80 (right) before and after the hydrothermal treatment in presence of a zirconium aqueous solution: a) FEB or MX-80; b) Zr-C-FEB-1 or Zr-C-MX-1; c) Zr-N-FEB-1 or Zr-N-MX-1; and; d) Zr-S-FEB-1 or Zr-S-MX-1.

Fig. 4. XRD of saponite before and after the hydrothermal treatment in presence of zirconium aqueous solution: a) SAP; b) Zr-C-SAP-1; c) Zr-N-SAP-1; and; d) Zr-S-SAP-1. *=zircon ($ZrSiO_4$) PDF 04-007-5058; o=cubic ZrO_2 PDF 04-015-0098; and; b=baddeleyite (monoclinic ZrO_2) PDF 00-037-1484
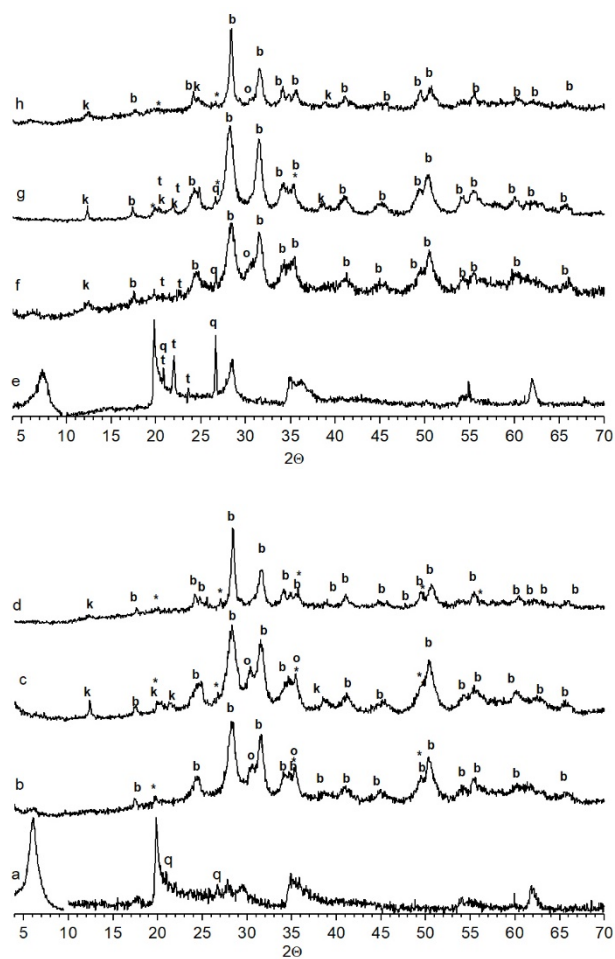
Fig. 5. ^{29}Si and ^{27}Al MAS NMR spectra of saponite before and after the hydrothermal treatment in presence of a zirconium aqueous solution: a) SAP; b) Zr-C-SAP-1; c) Zr-N-SAP-1; and; d) Zr-S-SAP-1.

494
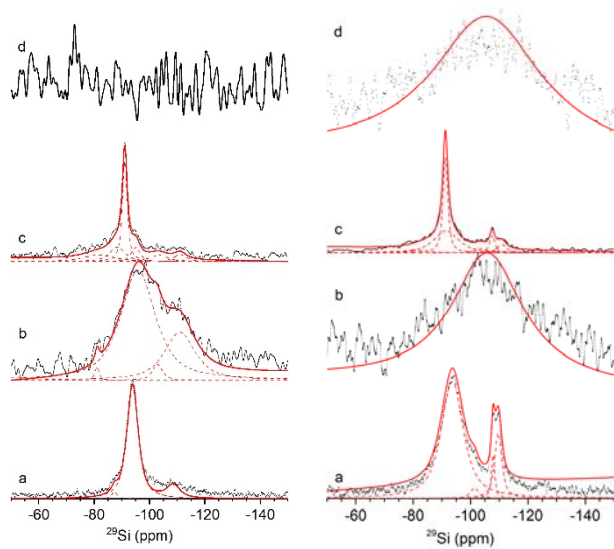495   **FIG. 1**
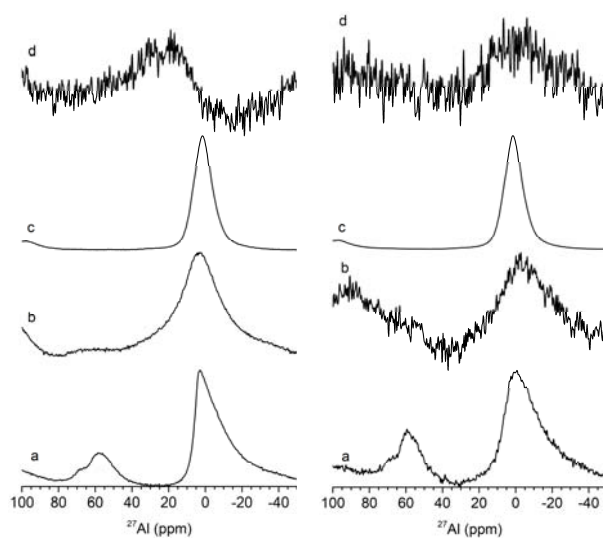496
497

23

498

499

500   **FIG. 2**

501

502

503

504

FIG. 3

FIG. 4

507

508

FIG. 5